

Cylindrical shape decomposition for 3D segmentation of tubular objects

Ali Abdollahzadeh^{a,*}, Alejandra Sierra^a, Jussi Tohka^a

^a*A.I. Virtanen Institute for Molecular Sciences, University of Eastern Finland, Kuopio, Finland*

Abstract

We develop a cylindrical shape decomposition (CSD) algorithm to decompose an object, which is a union of several tubular structures, into its semantic components. We decompose the object using its curve skeleton and translational sweeps. For that, CSD partitions the curve skeleton into maximal-length sub-skeletons over an orientation function, each sub-skeleton corresponds to a semantic component. To find the intersection of the tubular components, CSD translationally sweeps the object in decomposition intervals to identify critical points at which the shape of the object changes substantially. CSD cuts the object at critical points and assigns the same label to parts along the same sub-skeleton, thereby constructing a semantic component. CSD further reconstructs the semantic components between parts using generalized cylinders. We apply CSD for the segmentation of axons in large 3D electron microscopy images, and the decomposition of vascular networks, as well as synthetic objects. We show that CSD outperforms state-of-the-art decomposition techniques in these applications.

Keywords: object decomposition, cylindrical decomposition, generalized cylinder, tubular object, image segmentation, electron microscopy

1. Introduction

Shape decomposition is a fundamental problem in geometry processing in which an arbitrary object is regarded as an arrangement of simple primitives [1, 2] or semantic components [3, 4]. The application of shape decomposition mainly concerns disciplines such as object recognition and retrieval [5, 6], shape reconstruction [7], shape clustering [8], or modeling [9]. The application of shape decomposition in the context of image segmentation, however, is not well-studied. In this paper, we develop a decomposition algorithm called cylindrical shape decomposition (CSD) to apply for the segmentation of tubular structures in large 3D image datasets.

Recent advances in biomedical imaging have made possible acquiring three-dimensional (3D) images of unprecedented size, from gigabytes to hundreds of terabytes [10–12]. Typically, image segmentation of such datasets has been based on bottom-up strategies, where the image is first over-segmented into supervoxels, and subsequently, supervoxels are merged [13–15]. However, the process is error-prone because both the over-segmentation and subsequent merge are usually based

on local optimization as opposed to optimizing a global objective. In addition, the computational complexity of these methods depends on the number of supervoxels, which prohibitively increases time and memory consumption when encountering a big number (tens of thousands) of objects in large datasets. Our idea is instead to approach the segmentation problem based on a top-down strategy, where an under-segmentation is followed by the subsequent split using *a-priori* knowledge of the shapes to be segmented. This strategy enables dividing a large image dataset into sub-domains, geometry/topology of which can be analyzed based on a global objective. Also, these sub-domains can be processed independently and in parallel, addressing computation time and memory limitations. However, to manage the split operation, we need a new 3D shape decomposition algorithm.

Tubular structures are ubiquitous in biomedical image datasets: blood vessels in computed tomography angiography [10, 16] or neuronal structures in electron microscopy (EM) images [11, 17]. We apply a top-down design to segment tubular structures in large 3D image datasets. For that, we first enhance tubular structures in the 3D image dataset. Tubular structures can be enhanced on the foreground by curvilinear-enhancement filters, e.g., steerable filters [18, 19], orientation score-

*Corresponding author

based diffusion filters [20, 21], or machine learning techniques using deep-convolutional neural networks [22]. We assume that a thresholding-based preliminary segmentation of a 3D image with enhanced tubular structures includes under-segmented tubular objects. Therefore, we apply CSD to semantically decompose and correct the under-segmented tubular objects, i.e., subsequent split.

Figure 1b shows an under-segmented tubular object, i.e., an object that is a union of three tubular components (Fig. 1a). We propose to decompose the object into its semantic components using its curve skeleton and translational sweeps. For that, we determine the curve skeleton of the object: the union of several skeleton branches. We partition the curve skeleton of the object into maximal-length sub-skeletons over an orientation function. Each sub-skeleton corresponds to a semantic tubular component. In other words, skeleton branches are merged if they are thought to belong to the same semantic component. To identify intersections of the semantic components, we analyze the object cross-sections along its sub-skeletons, searching for critical points. A critical point is such a point that the object cross-section changes substantially. We restrict the translational sweep to intervals, called decomposition intervals, in the proximity of junction-points where skeleton branches connect. The object is cut at critical points to obtain object parts. We assigned the same label to the object parts along the same sub-skeleton to acquire a semantic component. We further reconstruct a semantic component at an intersection, using generalized cylinders. In this paper, our contributions are 1) an algorithm that partitions the skeleton graph of an object into distinct maximal-length paths over an orientation cost, 2) introducing decomposition intervals to restrict the translational sweeps, 3) using Hausdorff distance to calculate cross-sectional changes compared to an average curve directly, and 4) applying generalized cylinders to reconstruct the decomposed semantic components. We demonstrate the application of CSD in the segmentation of large 3D-EM datasets of myelinated axons, the decomposition of vascular networks, and synthetic objects. We also compare CSD to other state-of-the-art decomposition techniques: approximate convex decomposition [1] and skeleton-to-surface mapping [23]. These experiments indicate that CSD outperforms other decomposition techniques and achieves a promising performance. Fig. 1 compares our CSD method to approximate convex decomposition.

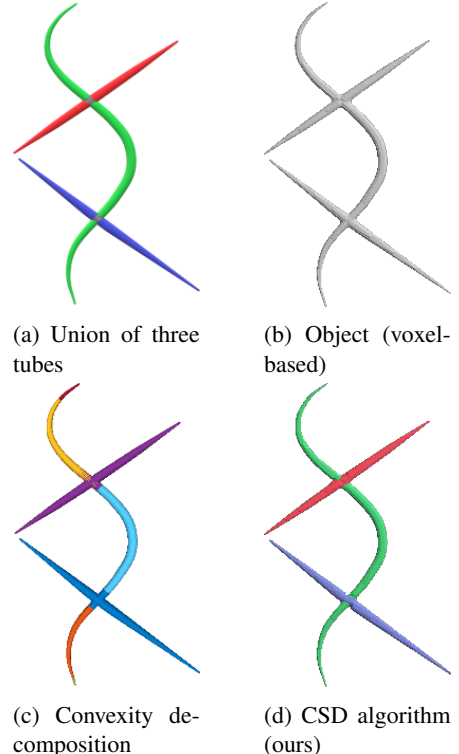


Figure 1: (a) A union of three tubular objects. The tubes are color-coded. The intersection of the tubes are colored grey. (b) A synthetic voxel-based object of size: $800 \times 400 \times 70$ voxels. (c) The approximate convex decomposition segmented the point cloud representation of the object into seven components. (d) Our method decomposed the object into three semantic tubular components.

2. Related works

Shape decomposition has been extensively studied in computer vision. In the following, we review the most relevant techniques. We distinguish between two types of shape decomposition techniques: 1) representing an object in terms of geometrically simple primitives, such as ellipsoids, generalized cylinders, or components with homogeneous characteristics [1, 2, 7, 24–28], and 2) decomposing an object into its semantic components using object skeleton or Reeb graph [3, 4, 23].

Simple primitives are homogeneous components with a compact representation and efficient computation. Examples of primitives with a simple parametric representation include ellipsoids [24] and straight cylinders [25]. Higher-level primitives such as tubular primitives [26], convex components [1, 27], generalized cylinders [2], and generalized sweep components [7, 28] can be generated by trading-off the representation simplicity, hence obtaining a smaller number of decomposition components. For example, tubular primitives in

Plumber [26] are constructed applying a seeded region growing with heuristically set of sphere positions and radii [26]. Plumber mainly extracts ideal tubular components of an object, and those object parts which are not classified as tubes are defined as body-parts of the object [26]. Convexity-based methods are an interesting class of primitive-based decomposition techniques. These techniques were developed based on the human tendency of dividing objects into parts around concave regions [29]. The approximate convex components in [1] were merged on a volumetric consistency measure to form semantic parts. The merging objective, however, does not address local volumetric differences within a semantic component and over-segments objects. Generalized cylinder decomposition is an alternative to the convex decomposition, quantifying cylindricity. Zhou *et al.* [2] introduced a quantitative measure for the cylindricity following the minimum description length principle [30] as a measure of the skeleton straightness and the variation among the profiles. The global objective for merging local generalized cylinders is to minimize the cylindricity. The approach yields excellent decomposition in synthetic objects. However, applying the method on large objects from biomedical images is computationally expensive for two reasons: 1) a large number of generalized cylinders should be fit into the object iteratively, and 2) a large number of generated generalized cylinders should be merged to satisfy the cylindricity objective. Another set of primitives-based decomposition techniques is based on cross-sectional sweeping. These algorithms, computationally less demanding compared to the convexity and generalized cylinder methods, sweep an object to generate homogeneous sweeping components. Goyal *et al* [7] study generates local prominent cross-sections from initial seed points. This method is semi-automated and requires user interactions for varying the density of the cross-sections in different regions of an object, and also for avoiding the creation of prominent cross-sections in regions with no sweep evidence. As well, at intersections, this method generates partial cross-sections, increasing the number of components. Li *et al.* [28] study is based on sweeping the object along its curve skeleton in search of critical points. In this method, the geometric function over which cross-sectional changes are measured is the perimeter of cross-sections, which is overly sensitive to the surface noise. As well, in the absence of an objective to merge local object parts, this method can over-segment the object to all surface protrusions.

To decompose an object into its semantic components, we can use the curve skeleton or Reeb graph of an object. Both concepts are object descriptors, and

they can guide the decomposition. The curve skeleton is a 1D representation of a 3D object [31], encoding its topology and geometry. The Reeb graph tracks topology changes in level sets of a scalar function [31]. Reniers *et al.* [23] developed a multi-scale skeleton extraction technique based on a global importance measure. The authors provided an object decomposition by defining skeleton-to-boundary mapping based on the shortest geodesics. The distance-based mapping, however, does not provide accurate boundaries between object parts. Au *et al.* [3] extract the curve skeleton by applying an implicit Laplacian smoothing with global positional constraints preserving the mesh connectivity and key features. The authors provide an object decomposition with an approximate measure of thickness about extracted curve skeletons. The method automatically assigns a cut to every skeleton branch, or semi-automatically enables the user to specify the desired number of segments. The automatic one-to-one assignment yields a sensitive decomposition to the skeletonization process, which is prone to having spurious branches. Berretti *et al.* [4] achieves the decomposition of a 3D mesh based on Reeb graph construction and refinement. The Reeb graph captures the surface topology and protrusions, and the refinement step uses curvature information and adjacency to the graph critical points to localize part boundaries. The boundaries, however, are not minimized over internal energy to generate smooth cuts.

3. Preliminary definitions

In this section, we define the core concepts used in the paper as there are no generally accepted definitions for most of them.

Object. An object $\Omega \subset \mathbb{R}^3$ is a nonempty bounded open set. We assume that its boundary $\partial\Omega$ is homeomorphic to a 2-sphere. For a discrete object, which is a result of a foreground segmentation, we define a 3D binary image as $I : X \subset \mathbb{Z}^3 \rightarrow \{0, 1\}$, and a segmented object $\Omega := \{x \in X : I(x) = 1\}$, where X is the image domain. Throughout the paper, Ω , $\partial\Omega$, and x are in \mathbb{R}^3 unless defined otherwise.

Curve skeleton. Given Ω and $\partial\Omega$, the curve skeleton $\Upsilon \subset \Omega$ is defined as a locus of centers of maximal inscribed balls [32]. A ball $B(x, r)$ centered at $x \in \Omega$ with radius r is maximally inscribed if its surface touches $\partial\Omega$ in at least two distinct points. Formally, B is a maximal inscribed ball in Ω if $\forall B', B \subseteq B' \subseteq \Omega \Rightarrow B' = B$.

Curve skeleton point type. We distinguish three types of points on the curve skeleton of an object: 1) regular-points that have exactly two neighbor points on

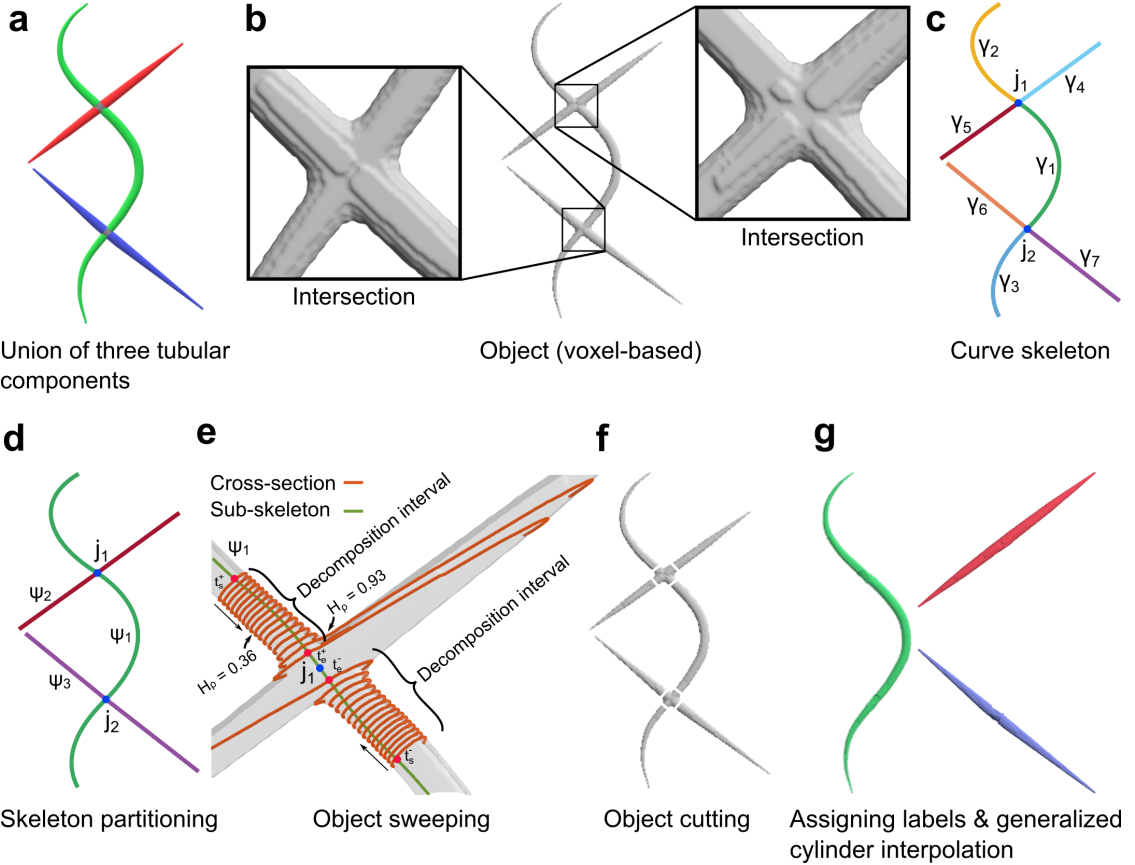


Figure 2: Outline of the CSD algorithm. (a) An object is a union of several tubular components. The tubular components are color-coded. (b) Voxel-based representation of the object. Intersections of the tubular components are magnified. (c) The curve skeleton of the synthetic object in (b) is the union of all skeleton branches. Skeleton branches are color-coded and denoted as γ . We defined a junction-point j as such a point that skeleton branches connect. Junction-points are shown as blue filled-circles. (d) The curve skeleton of the object is partitioned into maximal-length sub-skeletons ψ over a local orientation cost. The sub-skeletons are color-coded. (e) On a sub-skeleton ψ and in the proximity of a junction-point $j \in \psi$, we defined two decomposition intervals. The boundaries of decomposition intervals are shown with red filled-circles. In each interval, the object was swept along ψ and towards the joint j to find a critical point. At a critical point, the normalized Hausdorff distance H_ρ between a cross-sectional contour and the mean of visited cross-sectional contours exceeds θ_H . Sweeping directions are shown with arrows. (f) We cut the object at critical points to obtain object parts. (g) The object parts along the same sub-skeleton were assigned the same label to construct a semantic-component. The semantic-components were further reconstructed between their comprising object-parts using generalized cylinders. The synthetic object in (a) comprised of seven object-parts, and our algorithm decomposed it into three semantic-components.

the skeleton, 2) end-points that have exactly one neighbor point on the skeleton, and 3) junction-points that have three or more neighbor points on the skeleton [31].

We denote the collection of junction-points as J where $j \in J$ and the collection of end-points as O where $o \in O$.

Skeleton branch. Removing junction-points J from the curve skeleton Υ results in disconnected simple curves, known as skeleton branches. The collection of skeleton branches is denoted as Γ , and a skeleton branch is $\gamma \in \Gamma$. For $\gamma(t) : [0, 1] \rightarrow \mathbb{R}^3$, its arc-length is written as $l = \int_0^1 |\dot{\gamma}(t)| dt$ with the convention $\dot{\gamma}(t) := \frac{d}{dt} \gamma(t)$.

Skeleton graph. The topology of curve-skeleton Υ can be represented as a connected acyclic undirected graph (i.e., a tree) $G_\Upsilon = (V, E, L)$. There is a one-to-one map between skeleton branches in Γ and edges in E and a one-to-one map between the union of end and junction-points ($O \cup J$) and vertices in V . This means that for each branch $\gamma \in \Gamma$ we associate exactly one edge in $e \in G_\Upsilon$. $L \subset \mathbb{R}^+$ is the set of edge lengths. The length of an edge is the arc-length of its associated skeleton branch.

Walk, path. A walk is a finite or infinite sequence of edges which joins a sequence of vertices. A finite walk is a sequence of edges $W = \{e_1, e_2, \dots, e_{n'}\}$ for which there is a sequence of vertices $\{v_0, v_1, \dots, v_{n'}\}$ such that $e_i = v_{i-1}v_i$ for $i = 1, \dots, n'$. The vertex sequence of the walk is $(v_0, v_1, \dots, v_{n'})$. A path is a walk in which all vertices are distinct.

Sub-skeleton is a path in the curve skeleton domain. If $W = \{e_1, e_2, \dots, e_{n'}\}$ is a path in the skeleton graph, and $\{\gamma_1, \gamma_2, \dots, \gamma_{n'}\}$ are corresponding skeleton branches, then $\psi = \cup_i \gamma_i \subseteq \Upsilon$ is a sub-skeleton.

Critical point. A point on a sub-skeleton at which the cross-sectional contour of the object changes substantially. We provide a formal definition in section 6.2.

Cut. A closed simple curve $C \subset \partial\Omega$ is a cutting-curve if $\partial\Omega \setminus C$ is not connected. Cut means removal of a cutting-curve from the surface.

4. Outline of the CSD algorithm

The outline of the CSD algorithm is shown in Fig. 2, and it is as follows:

1. Define the curve skeleton of a given object (Fig. 2c, section 5.1).
2. Partition the curve skeleton of the object into sub-skeletons (Fig. 2d, section 5.2).
3. Define decomposition intervals to restrict the object sweep (Fig. 2e, section 6.1).

4. Sweep the object to find critical points and cut the object at critical points (Fig. 2e and Fig. 2f, section 6.2).
5. Reconstruct the object between parts that have the same label using generalized cylinders (Fig. 2g, section 7).

5. Skeleton partitioning

We use the curve skeleton of an object to drive the decomposition. For that, we partition the skeleton graph into several distinct paths union of which covers the skeleton graph. The partitioning of the skeleton graph, by extension, partitions the curve skeleton into sub-skeletons. Each sub-skeleton corresponds to exactly one semantic object component.

5.1. Curve skeleton

To determine the curve skeleton of an object Ω with sub-voxel precision, we apply a method from [33, 34]. The algorithm initiates by determining a point $x^* \in \Omega$ with the largest distance from the object surface $\partial\Omega$ inside the object domain. This point is used to determine a skeleton branch $\gamma(t) : [0, 1] \rightarrow \mathbb{R}^3$, starting at x_s , the furthest geodesic point from x^* in Ω , and ending at x^* . A cost function F is defined to enforce the path to run in the middle of Ω , where F should increase if the path moves away from the center. To determine F , we find the distance field $D(x)$ from $\partial\Omega$, and assign $F = 1 - (\frac{D(x)}{D(x^*)})^2$. The distance field $D(x)$ is determined by solving an Eikonal equation on the object domain Ω using the fast marching method [35]. Starting at x_s , the skeleton branch γ is traced by a back-tracking procedure on F to reach x^* , written as

$$\gamma = \arg \min_P \int_{x_s}^{x^*} F(P(t)) dt, \quad (1)$$

where t traces the path P . For the back-tracking procedure, we use the Euler scheme, which solves the ordinary differential equation with a sub-voxel accuracy. This process is repeated to determine further branches that form the curve skeleton of the object. But rather than using the single point x^* as the start point for the fast marching method, all points in the previously calculated branches are used as start points. We propagate a new wave from the start points with the speed F to update x_s . The point x_s is now the furthest point from the current state of the curve skeleton and the start point of the new branch. Applying a back-tracking algorithm from the updated x_s defines the new skeleton branch.

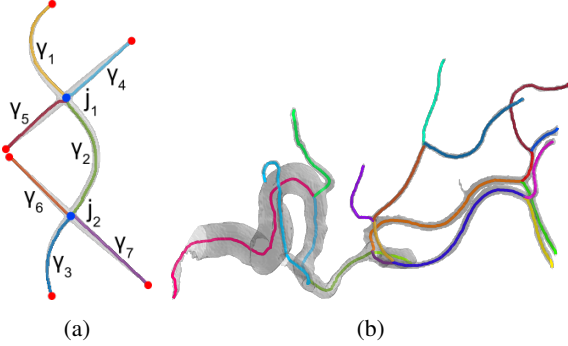


Figure 3: The curve skeleton of an object is the union of all skeleton branches. (a) The skeleton of the synthetic object, size: $800 \times 400 \times 70$ voxels, 7 branches. The blue filled-circles show junction-points, and the red filled-circles show end-points. The skeleton graph of this object is $G_T(V, E, L)$, where $E = \{e_1, \dots, e_7\}$, $V = \{v_0, \dots, v_7\}$, and $L = \{l_1, \dots, l_7\}$. (b) The skeleton of a vascular network, size: 256×256 voxels, 20 branches. Skeleton branches are color coded.

Figure 3 shows the skeletons of a synthetic object and a vascular network.

5.2. Skeleton graph decomposition

Several skeleton branches are often required to represent one semantic component of an object, and therefore detecting skeleton branches is not sufficient for a semantic decomposition. An example is shown in Fig. 3a, where the union of three skeleton branches γ_1 , γ_2 , and γ_3 is required to represent one tubular component. To formalize what constitutes a semantic decomposition, we consider connectivity, length, and local orientation, to unify skeleton branches. We propose an algorithm for traversing the graph representation of the curve skeleton $G_T(V, E, L)$, decomposing G_T into distinct paths, each corresponds to a semantic component. The algorithm starts at the root edge and explores as far as possible along edges which provide the optimal choice at each stage.

We partition the skeleton graph of the object into several distinct paths union of which covers the set of graph edges. Formally, we partition $G_T(V, E, L)$ into m paths $W_i, i = 1, \dots, m$ so that $\cup_i W_i = E$ and $W_i \cap W_k = \emptyset \forall i, k = 1, \dots, m, i \neq k$. To determine the paths, we require four conditions: 1) the path contains the longest edge not associated to any other path, 2) the path has the maximum number of edges, 3) the associated angle between two successive edges is bigger than θ_c , and 4) the path locally minimize an orientations cost. Denoting two successive edges in a path as e_s and e_{s+1} , the edge e_{s+1} has the maximum angle compared to e_s among the set of connected edges to e_s . The angle between two edges e_s and e_{s+1} is the angle between the line segments

```

Input :  $G_T = (V, E, L); \theta_c$ .
Output: Collection of distinct paths  $\Lambda$ .
 $\Lambda \leftarrow \emptyset$ 
while  $E \neq \emptyset$  do
   $W \leftarrow \emptyset; e^* \leftarrow$  longest  $e \in E$ 
   $V^* \leftarrow \{ \text{incident vertices to } e^* \}$ 
   $W \leftarrow W \cup \{e^*\}$ 
  forall  $v \in V^*$  do
     $e^{ref} \leftarrow e^*$ 
     $v^{next} \leftarrow v$ 
    while  $\deg(v^{next}) > 1$  and  $e^{ref} \neq \emptyset$  do
       $CE \leftarrow \{ \text{edges connected to } v^{next} \} \setminus e^{ref}$ 
       $e^{next} \leftarrow \emptyset$ 
      forall  $e^{ngb} \in CE$  do
         $\theta_{max} \leftarrow \theta_c; \theta \leftarrow \angle(e^{ref}, e^{ngb})$ 
        if  $\theta > \theta_{max}$  then
           $\theta_{max} \leftarrow \theta; e^{next} \leftarrow e^{ngb}$ 
        end
      end
       $e^{ref} \leftarrow e^{next}$ 
      if  $e^{ref} \neq \emptyset$  then
         $v^{next} \leftarrow v_2, \text{ where } e^{ref} = (v_2, v^{next})$ 
         $W \leftarrow W \cup \{e^{ref}\}$ 
      end
    end
  end
   $\Lambda \leftarrow \Lambda \cup \{W\}$  and  $E \leftarrow E \setminus W$ 
end

```

Algorithm 1: Decomposing the set of edges of G_T into distinct paths. A vertex and an edge are called incident if the vertex is one of the two vertices the edge connects.

connecting endpoints of the skeleton branches associated with edge e_s and e_{s+1} , and it lies in range $[0, \pi]$. We used Algorithm 1 to determine the m distinct paths on G_T . Figure 4 shows skeleton graph decomposition of the synthetic object $n = 7$ into three paths $m = 3$. Each path is equivalent to a sub-skeleton.

6. Cylindrical decomposition

In this section, we propose a method to decompose an object into parts and intersections by cutting the object at critical points. To determine critical points, we sweep the object along sub-skeletons in decomposition intervals to find locations where the object geometry changes substantially (see Fig. 6).

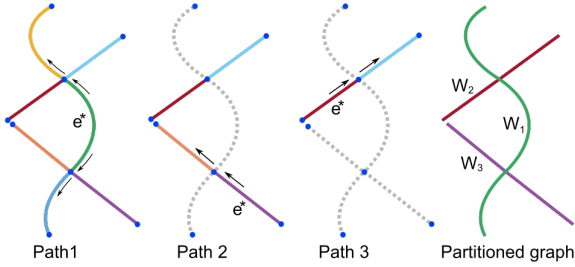


Figure 4: Partitioning the skeleton graph of the synthetic tubular object. E comprises 7 edges and is partitioned into 3 paths: $W_1 = \{e_1, e_2, e_3\}$, $W_2 = \{e_4, e_5\}$, and $W_3 = \{e_6, e_7\}$. We determine W_1 starting from the longest edge in E denoted as e^* towards its incident vertices. At each vertex, we traverse the edge with minimum orientation cost. Appending new edges terminates when a leaf vertex is visited or the angle between two successive edges is smaller than θ_c . We subtract W_1 from E , when W_1 is determined (see Algorithm 1). The blue filled-circles show vertices in G_T . The edges are color coded with full-lines. At vertices, arrows show where to traverse next when standing on e^* . The grey dash-lines show the previously calculated paths.

6.1. Decomposition interval

We restrict the sweep of the object along each sub-skeleton to decomposition intervals in the proximity of a junction-point j on sub-skeleton ψ as illustrated in Fig. 5b. It is convenient to work with parametrized sub-skeleton $\psi(t) : [0, 1] \rightarrow \mathbb{R}^3$. We define two decomposition intervals $[t_s^+, t_e^+]$ and $[t_e^-, t_s^-]$ for each junction-point as in Fig. 5a. To determine the boundaries of a decomposition interval, we define an upper threshold r_s and a lower threshold r_e . We specify r_s and r_e based on the radius of the maximal inscribed ball at t_j and two factors $\alpha_s \geq 1$ and $\alpha_e \geq 0$ where $\alpha_s \geq \alpha_e$, as $r_s = \alpha_s \times r$ and $r_e = \alpha_e \times r$.

To determine the thresholds, we use the signed arc-length from j . Define t_j so that $j = \psi(t_j)$. Then $t_s^+(t_s^-)$ is such a point on the sub-skeleton that signed arc-length from t_j to $t_s^+(t_s^-)$ equals r_s ($-r_s$). And $t_e^+(t_e^-)$ is such a point on the sub-skeleton that signed arc-length from t_j to $t_e^+(t_e^-)$ equals r_e ($-r_e$). We have $t_s^+ < t_e^+ < t_j < t_e^- < t_s^-$.

The upper and lower thresholds may imply arc-distances outside parametrization limits of ψ . If the arch-length from $\psi(0)$ to $\psi(t_j)$ is smaller than r_s (r_e) we assign $t_s^+ = 0$ ($t_e^- = 0$). And if the arch-length from $\psi(t_j)$ to $\psi(1)$ is smaller than r_s (r_e) we assign $t_s^- = 1$ ($t_e^- = 1$). Also, when a junction-point is at the either ends of a sub-skeleton, e.g., in a T-shape object, we define only one decomposition interval. Therefore, if $\psi(t_j) = 0$ ($\psi(t_j) = 1$) the only interval that we define is $[t_e^-, t_s^-]$ ($[t_s^+, t_e^+]$). Figure 5b shows decomposition intervals in

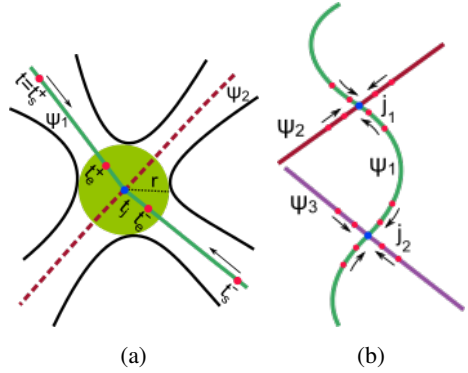


Figure 5: (a) In the proximity of every junction-point, e.g. j_1 blue filled-circle, and on each sub-skeleton, e.g. ψ_1 green line, we define two decomposition intervals, $[t_s^+, t_e^+]$ and $[t_e^-, t_s^-]$, tracing ψ_1 , from t_s^+ to t_e^+ and from t_e^- to t_s^- (red filled-circles). The lower and upper bounds of the intervals are two factors of the radius of the maximal inscribed ball at t_j , the green circle. (b) Decomposition intervals in the proximity of all junction-points j_1 and j_2 and for all sub-skeletons ψ_1, ψ_2 , and ψ_3 are defined with the red filled-circles. Only in decomposition intervals, we are allowed to sweep the object. Arrows depict the sweeping direction to approach junction-points.

the proximity of j_1 and j_2 on sub-skeletons ψ_1, ψ_2 , and ψ_3 .

6.2. Critical point

A critical point on a sub-skeleton is such a point that the cross-sectional contour of the object at this point changes substantially (Fig. 6). We use the Hausdorff metric to compare geometrical changes between cross-sectional contours in a decomposition interval. The Hausdorff distance between two curves C_1 and C_2 is calculated as

$$\mathcal{H}(C_1, C_2) = \max\{\sup_{p \in C_1} \inf_{q \in C_2} d(p, q), \sup_{p \in C_2} \inf_{q \in C_1} d(p, q)\}, \quad (2)$$

where $d(\cdot)$ is the Euclidean distance between two points. We sweep $\partial\Omega$ by a cross-sectional plane $\mathcal{P} \subset \mathbb{R}^3$ to extract the cross-sectional contours. A cross-sectional plane $\mathcal{P}(t)$ is a plane orthogonal to ψ at every point t along ψ . The plane normal is equal to the tangent vector to ψ at point $\psi(t)$. We sweep $\partial\Omega$ by \mathcal{P} along ψ in $[t_s^+, t_e^+]$ interval starting at t_s^+ toward t_e^+ , and in $[t_e^-, t_s^-]$ interval starting at t_e^- toward t_s^- as illustrated in Fig. 5a. Let $\mathcal{P}(t)$ intersects $\partial\Omega$ at an inquiry point t . Since we assumed that $\partial\Omega$ is homeomorphic to a 2-sphere, the cross-sectional contour $C(\zeta) : [0, 1] \rightarrow \mathbb{R}^2$ is a simple closed curve, where $C(0) = C(1)$. Translating \mathcal{P} along $\psi(t)$ with t moving in decomposition intervals, we compare the Hausdorff distance between the cross-sectional

contour at t denoted as C_t with the average of visited cross-sectional contours μ .

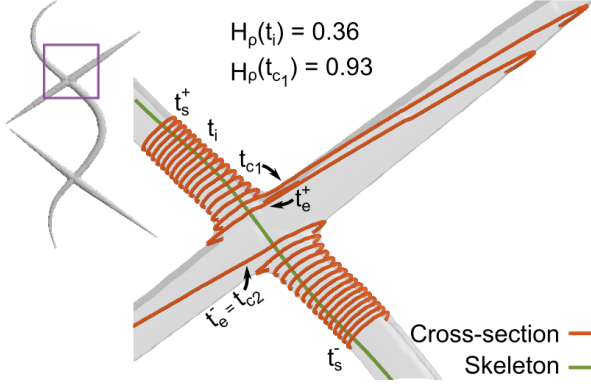


Figure 6: Sweeping the object surface along the sub-skeleton ψ_1 at junction-point j_1 between $[t_s^+, t_e^+]$ and $[t_s^-, t_e^-]$. At any decomposition interval, if $H_\rho < \theta_H$ the inquiry continues to the next point. If $H_\rho(t) \geq \theta_H$ the inquiry stops at t and the point is called a critical point. The critical point in the first interval is denoted as t_{c1} and in the second interval as t_{c2} .

To find the average curve μ between two nearly similar curves C_1 and C_2 , we first need a one-to-one mapping between C_1 and C_2 . We use OrthoMap OM method from [36]. Consider that C_1 is parameterized by ς . To each point $C_1(\varsigma)$ of C_1 , the $OM(C_1, C_2)$ associates the closest point $C_2(\varsigma)$ on C_2 that lies on the line passing through $C_1(\varsigma)$ and having for direction the normal $N(\varsigma)$ to C_1 at $C_1(\varsigma)$. Having this mapping, then each point $C_2(\varsigma)$ of C_2 may be expressed as the normal offset $C_1(\varsigma) + d(\varsigma)N(\varsigma)$ of $C_1(\varsigma)$. We say that $C_1(\varsigma)$ is the closest normal projection of $C_2(\varsigma)$ onto C_1 and can express C_2 as a deformation of C_1 completely defined by the normal displacement field $d(\varsigma)$. The average curve obtained by OrthoMap correspondence is asymmetric: $OM(C_1, C_2)$ is not necessarily equal to $OM(C_2, C_1)$. Therefore, we consistently take C_1 as an already visited curve, C_2 as the new cross-sectional curve, and define the average curve over $OM(C_1, C_2)$.

We normalize the Hausdorff distance $\mathcal{H}(C_t, \mu)$ to the range $[0, 1]$ and denote it as $H_\rho(t)$. For that we first find a point interior to C_t denoted as κ . We define $\kappa \in \mathbb{R}^2$ to be the intersection of \mathcal{P} and ψ at point t . Defining $d_{C_t}(\kappa) = \sup_{q \in C_t} d(\kappa, C_t)$, we write $H_\rho(t)$ as

$$H_\rho(t) = \frac{\mathcal{H}(C_t, \mu)}{\mathcal{H}(C_t, \mu) + d_{C_t}(\kappa)}. \quad (3)$$

We define a similarity threshold between cross-sectional contours as θ_H . While sweeping $\partial\Omega$ along ψ from t_s^+ (t_s^-) to t_e^+ (t_e^-), if $H_\rho(t) < \theta_H$, the inquiry continues to the next point. However, if $H_\rho(t) \geq \theta_H$ the inquiry

stops at t and the point is called a critical point, denoted as t_{c1} (t_{c2}) as shown in Fig. 6. In $[t_s^+, t_e^-]$ ($[t_e^-, t_s^-]$), if at no inquiry point $H_\rho(t)$ exceeds θ_H , we define the t_{c1} (t_{c2}) as the point with minimum arc-distance r ($-r$) to $\psi(t_j)$ at which H_ρ is maximum.

7. Object reconstruction

We cut the object at all critical points and decompose $\partial\Omega$ into n parts, n is the number of skeleton branches, and δ intersections, δ is the number of junction-points. We distinguish between an object part and an intersection such that the interior of an intersection includes a junction-point. The final decomposition step is to discard intersections and assign the same label to those object parts that are along the same sub-skeleton to obtain m semantic tubular components, m is the number of sub-skeletons. As we discard the intersections, we reconstruct the semantic tubular components using generalized cylinders. A generalized cylinder $\Phi(u, \varsigma) : [0, 1]^2 \rightarrow \mathbb{R}^3$ represents an elongated surface on an arbitrary axis and smoothly varying cross-sections [37]. In Cartesian coordinates x_1, x_2, x_3 , the axis is parametrized by u as $\zeta(u) = (x_1(u), x_2(u), x_3(u))$ and cross-section boundary is represented as $C_u(\varsigma) = (x_1(u, \varsigma), x_2(u, \varsigma))$. To construct Φ , we apply a translational sweep along $\zeta(u)$ using closed simple curves $C_u(\varsigma)$ written as

$$\Phi(u, \varsigma) := \{\zeta(u) \in \mathbb{R}^3, C_u(\varsigma) \in \mathbb{R}^2 : u, \varsigma \in [0, 1]\}. \quad (4)$$

To obtain a parametric representation of generalized cylinders, it is convenient to employ a local coordinate system defined with the origin at each point of $\zeta(u)$. A convenient choice is the Frenet-Serret frame which is suitable for describing the kinematic properties of a particle moving along a continuous, differentiable curve in \mathbb{R}^3 . The Frenet-Serret frame is an orthonormal basis composed of three unit vectors e_T , e_N , and e_B , where e_T is the unit tangent vector, and e_N and e_B are the unit normal and unit binormal vectors, respectively. By defining the cross-section in the Frenet-Serret frame, we form a parametric representation of generalized cylinders [38] as follows:

$$\Phi(u, \varsigma) = \zeta(u) + x_1(u, \varsigma)e_N(u) + x_2(u, \varsigma)e_B(u) \quad (5)$$

To define $C_u(\varsigma)$, we use homotopy between two curves $C_{c1}(\varsigma)$ and $C_{c2}(\varsigma)$, where the curves are obtained by cross-sectioning the object surface at critical points t_{c1} and t_{c2} , respectively (see Fig. 7a). Let the simple

closed curves $C_{c_1}(\zeta)$ and $C_{c_2}(\zeta)$ in \mathbb{R}^2 be homotopic with a continuous map $h : [0, 1]^2 \rightarrow \mathbb{R}^2$. So, we write:

$$h(0, \zeta) = C_{c_1}(\zeta), h(1, \zeta) = C_{c_2}(\zeta), \forall \zeta \in [0, 1], \quad (6)$$

$$h(u, 0) = h(u, 1), \forall u \in [0, 1], \quad (7)$$

where h is called a homotopy from $C_{c_1}(\zeta)$ to $C_{c_2}(\zeta)$. We denote a cross-section at a point along $\zeta(u)$ as $C_u := h(u, \cdot)$. Note that, \mathbb{R}^2 is simply connected space. We use a linear homotopy between $C_{c_1}(\zeta)$ to $C_{c_2}(\zeta)$ defined as:

$$h(u, \zeta) = (1 - u) C_{c_1}(\zeta) + u C_{c_2}(\zeta), \quad (8)$$

where the computation on the right side is in \mathbb{R}^2 . Equation 8 essentially indicates that we are moving from $C_{c_1}(\zeta)$ to $C_{c_2}(\zeta)$ along a straight lines. To define the curve $\zeta(u)$, we use an interpolation between $\psi(t_{c_1})$ and $\psi(t_{c_2})$. Figure 7b shows Φ on different choices of ζ .

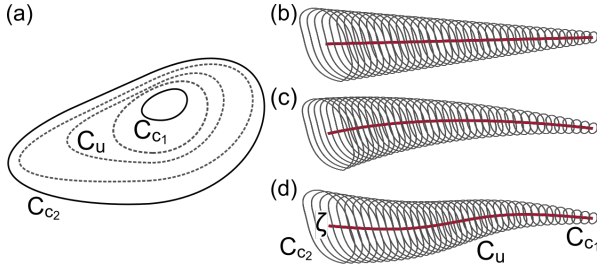


Figure 7: (a) Homotopy between two curves $C_{c_1}(\zeta)$ and $C_{c_2}(\zeta)$. Generalized cylinder along (b) a linear, (c) spline, and (d) sine interpolation between $\psi(t_{c_1})$ and $\psi(t_{c_2})$.

8. Experimental results

In this section, we evaluate the effect of different parameters on the decomposition, present CSD application in the decomposition of tubular objects in biomedical images, and show its performance for more general objects.

8.1. Parameter setting

In our experiments, we fix the value of $\alpha_e = 1$ (defined at section 6.1) which means that t_e^+ (t_e^-) is a point such that its distance to a junction-point is equal to the radius of the maximal inscribed ball at that junction-point. We examine the effect of α_s (defined at section 6.1) which determines t_s^+ (t_s^-) in decomposition intervals and set $\theta_H = 0.7$, the similarity threshold (defined at section 6.2). We use a linear interpolation for defining ζ , a curve on which a generalized cylinder is defined (defined at section 7), and set $\theta_c = 0^\circ$, an angle that the associated angle between two successive

edges is bigger than it (defined at section 5.2). Figure 8 shows the decomposition of the synthetic tubular object at $\alpha_s = 10, 20, 30$. For smaller values of α_s sweeping the object starts from points closer to junction-points. The decomposition/reconstruction at $\alpha_s = 10$ is faithful to the original object because the critical points are detected close to the junction-points. However, when α_s is equal to 30, CSD does not tolerate gradient changes of the tube diameter. This suggests that $\alpha_s = 30$ is a big value for starting the cross-sectional sweep. Setting α_s to small values provides more accurate decomposition results, but it also increases the risk that the cross-sectional sweep starts at a point very close to the junction, resulting in inaccurate identification of intersections. This is important when we apply CSD on tubular objects extracted from biomedical images, because 1) a preliminary foreground segmentation contains surface noise, and 2) the curve skeleton may not exactly lie in the center of the object. In both cases, the radius of the maximum inscribed ball at a junction-point can be measured smaller than its true value. For α_s and α_e , we suggest values in range [5, 20] and [0.5, 2], respectively.

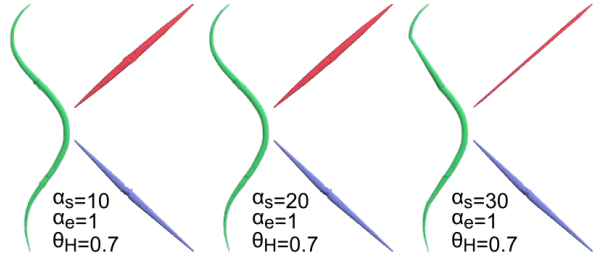


Figure 8: Decomposition of the synthetic tubular object at $\alpha_s = 10, 20, 30$ for fixed values of $\alpha_e = 1, \theta_H = 0.7$. We use a linear interpolation to define ζ and set $\theta_c = 0^\circ$. At $\alpha_s = 10$, the decomposition is accurate because critical points are detected close to the junction-points. Increasing the value of α_s to 30, CSD does not tolerate gradient changes of the tube diameter, hence recognizes critical points at distant locations from junction-points.

We also examine the effect of θ_H , which determines the similarity threshold between a cross-sectional contour and μ . Figure 9 shows the decomposition of the synthetic object at $\theta_H = 0.6, 0.7, 0.8$. To better demonstrate the effect of θ_H , we set $\alpha_s = 30$, which we earlier showed that the decomposition/reconstruction at that $\alpha_s = 30$ is not faithful to the original object. We set $\alpha_e = 1$ and used a linear interpolation to define ζ . We set $\theta_c = 0^\circ$. At $\theta_H = 0.6$, CSD is sensitive to the gradient increase of the tube diameter; hence the critical points are detected distant from junction-points. However, at $\theta_H = 0.7$ and $\theta_H = 0.8$ the tolerance of CSD to cross-sectional changes increases, thus the decom-

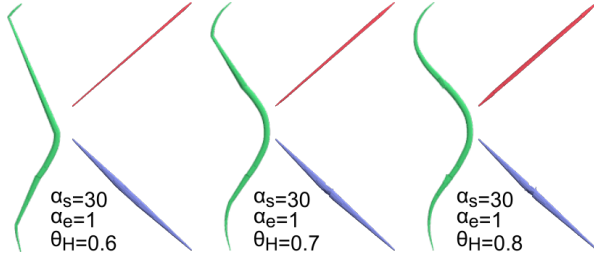


Figure 9: Decomposition of the synthetic tubular object at $\theta_H = 0.6, 0.7, 0.8$ for fixed values of $\alpha_s = 30$ and $\alpha_e = 1$. We use a linear interpolation to define ζ and set $\theta_c = 0^\circ$. Increasing the θ_H value increases the CSD tolerance in dealing with gradient cross-sectional changes of the tubes. At $\theta_H = 0.8$, CSD recognizes the critical points near to junction-points, despite distant starting points for the cross-sectional sweeping.

position becomes more accurate despite distant starting points for cross-sectional sweeping. Note that, increasing θ_H elevates the tolerance of CSD to the cross-sectional changes very quickly, e.g., at $\theta_H = 0.9$ the algorithm tolerates nine times difference between a cross-section and μ , and at $\theta_H = 0.95$, it tolerates 19 times difference. We suggest θ_H to be in range $[0.7, 0.85]$.

To partition the skeleton graph, we assume that at a vertex, the angle between two successive edges is bigger than θ_c . By setting θ_c to bigger values, we emphasize the straightness of a path, but then a path may not be maximal-length. Figure 10 shows how θ_c affects the number of semantic components. At $\theta_c = 0^\circ$, we obtain maximal-length paths and minimum number of object partitions (Fig. 10b). By increasing θ_c , fewer edges are allowed to append, which increases the number of object partitions. Figure 10c shows that decomposition for $\theta_c = 135^\circ$ yields 4 semantic components. At $\theta_c = 180^\circ$, every edge in the skeleton graph is a path, hence producing the maximum number of semantic components, which is equal to the number of skeleton branches, $m = 5$.

8.2. Axon segmentation in EM volumes

The main purpose of developing CSD is to segment tens of thousands of myelinated axons in large white matter 3D-EM datasets of size $4000 \times 2000 \times 1300$ voxels. We generate a probability map of myelinated axons using deep convolutional neural networks (for details, refer to [39]). We threshold the probability map, and using connected component analysis obtain a preliminary foreground segmentation of myelinated axons. Figure 11 (first column) shows examples of myelinated axons after connected component analysis with an under-segmentation error(s): an axon intersects other axons or merges with the extra-axonal space. We apply CSD

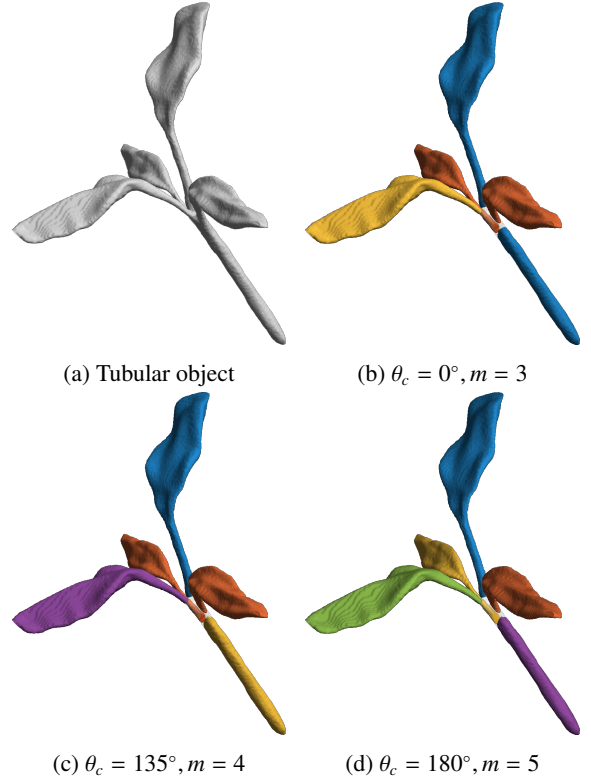


Figure 10: The angle between two successive edges in a path should be bigger than θ_c . (a) A synthetic tubular object, size: $300 \times 300 \times 300$ voxels. (b) Setting $\theta_c = 0^\circ$ produces maximal-length paths, minimum number of semantic components $m = 3$. (c) At $\theta_c = 135^\circ$, the number of semantic components increases to $m = 4$. (d) At $\theta_c = 180^\circ$, every edge in the skeleton graph is a path, hence producing the maximum number of semantic components, which is equal to the number of skeleton branches, $m = 5$.

to evaluate every preliminary segment for the under-segmentation error. If CSD recognizes the error in a preliminary segmented component, it decomposes the segmented component into its semantic components. Figure 11 shows the performance of CSD in decomposition of axons and also compares our method to the approximate convex decomposition [1] and skeleton-to-surface mapping [23] approaches. The approximate convex decomposition algorithm functions on point cloud representation of objects. To apply it on large objects, we first down-sample the point cloud representation of objects to 50 000 points, enabling the decomposition to be performed in a reasonable time (less than 10 minutes per object). Figure 11 (second column) shows that approximate convex method over-segments the objects. We perform skeleton-to-surface mapping decomposition based on Voronoi partitioning of the surface, using Euclidean distance to skeleton branches (Fig. 11 (third column)).

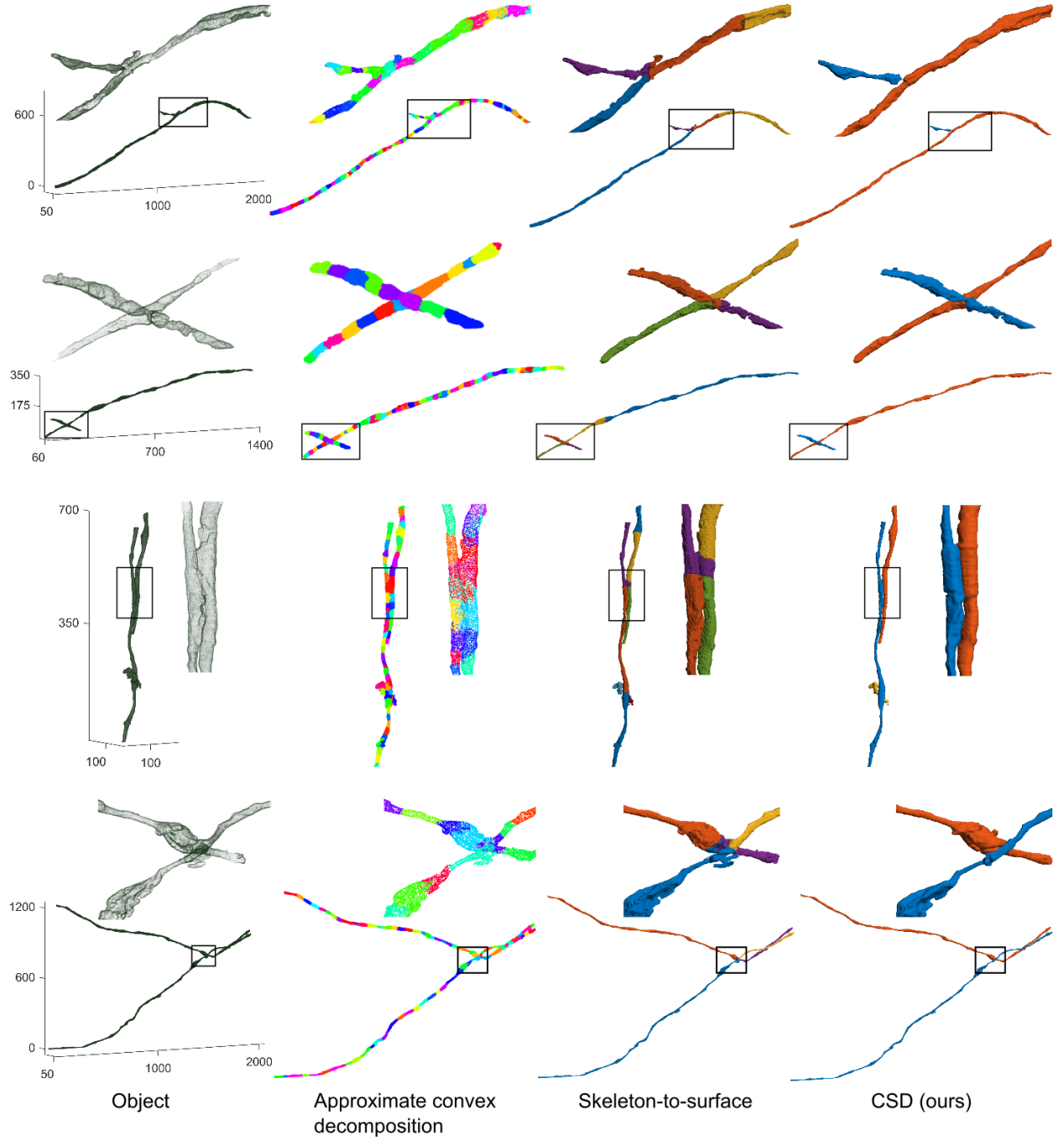


Figure 11: First column: examples of foreground segmentation of myelinated axons with under-segmentation. Second column: decomposition using the approximate convex method. The point cloud representation of objects is first down-sampled to 50 000 points to enable the decomposition task in a reasonable time. The method over-segments the objects. Third column: skeleton-to-surface mapping based on Voronoi partitioning of the surface using skeleton branches. Last column: CSD decomposition provides the correct number of semantic components in under-segmented myelinated axons. The objects are reconstructed at intersections using generalized cylinders ($\alpha_s = 10, \alpha_e = 1.5, \theta_H = 0.85$, spline interpolation to define $\zeta, \theta_c = 90^\circ$). Objects inside boxes are magnified.

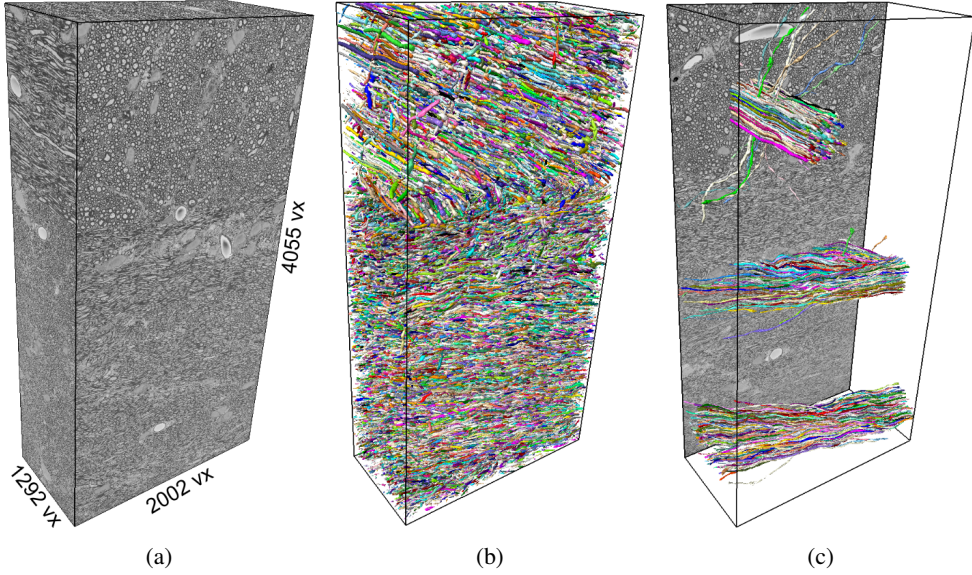


Figure 12: (a) A large 3D-EM dataset of the white matter. The size of the dataset is $4\,055 \times 2\,002 \times 1\,292$ voxels in x , y , and z directions, respectively. (b) A 3D rendering of myelinated axons (at one-third of the original resolution). CSD evaluates a preliminary segment for under-segmentation error(s), and if required, decomposes and reconstructs an under-segmented myelinated axon. (c) A 3D rendering of myelinated axons sampled at different locations illustrating the diversity of thickness and orientation in segmented axons.

Since the curve skeleton captures the geometry and topology of an object, skeleton-to-surface mapping decomposes the object close-to-semantic, but it does not recognize intersections for further object reconstruction. Figure 11 (last column) shows our decomposition of myelinated axons. CSD provides the correct number of semantic components in under-segmented myelinated axons. The objects are reconstructed at intersections using generalized cylinders ($\alpha_s = 10$, $\alpha_e = 1.5$, $\theta_H = 0.85$, spline interpolation to define ζ , and $\theta_c = 90^\circ$). Figure 12 shows the complete segmentation of myelinated axons in a large 3D-EM dataset, where CSD scans, decomposes, and reconstructs about 30 000 myelinated axons.

8.3. Decomposition of vascular networks

We examine our method, approximate shape decomposition [1], and skeleton-to-surface mapping on a vascular network (acquired from https://github.com/cbm755/fast_marching_kroon), as shown in Fig. 13a. Figure 3b shows 20 skeleton branches extracted from the vascular network. Figure 13b shows that approximate convex decomposition over-segments the vascular network. Figure 13c shows that skeleton-to-surface mapping decomposes the object into 20 semantic components based on the Euclidean distance to skeleton benches, but the method does not identify intersections. For example, Fig. 13c (magnified box) shows that where the thin vessel (green partition) bends on the

thick vessel (red partition), skeleton-to-surface mapping erroneously assigns a section of the thick vessel to the thin vessel; the section which has a smaller distance to the skeleton of the thin vessel. CSD decomposes the object into eight semantic components and reconstructs the object at intersections ($\alpha_s = 4$, $\alpha_e = 1$, $\theta_H = 0.85$, spline interpolation to define ζ , $\theta_c = 90^\circ$).

8.4. Decomposition of synthetic objects

To demonstrate the general applicability of our algorithm, we examine CSD on synthetic objects with voxel-based representation from McGill 3D Shape Benchmark [6]. These objects have a wider sense of tubularity, e.g., tables or birds are composed of flat object parts. We decompose the objects by increasing the length of decomposition intervals, bigger values of α_s , smaller values of α_e , increasing θ_H to tolerate bigger cross-sectional changes, and dropping the object reconstruction step. Figure 14 shows a gallery of decomposition on a mixture of objects with articulating parts, such as humans, spiders, pliers, and objects with moderate articulation, such as tables, and dinosaurs, and airplanes. A grey-colored partition in decomposed objects of Fig. 14 depicts the intersections. Table 1 demonstrates how many object parts, n , semantic components, m , intersections, δ , are extracted from different objects. Also, Table 1 shows the computation time for the determination of the object curve skeleton and its critical points.

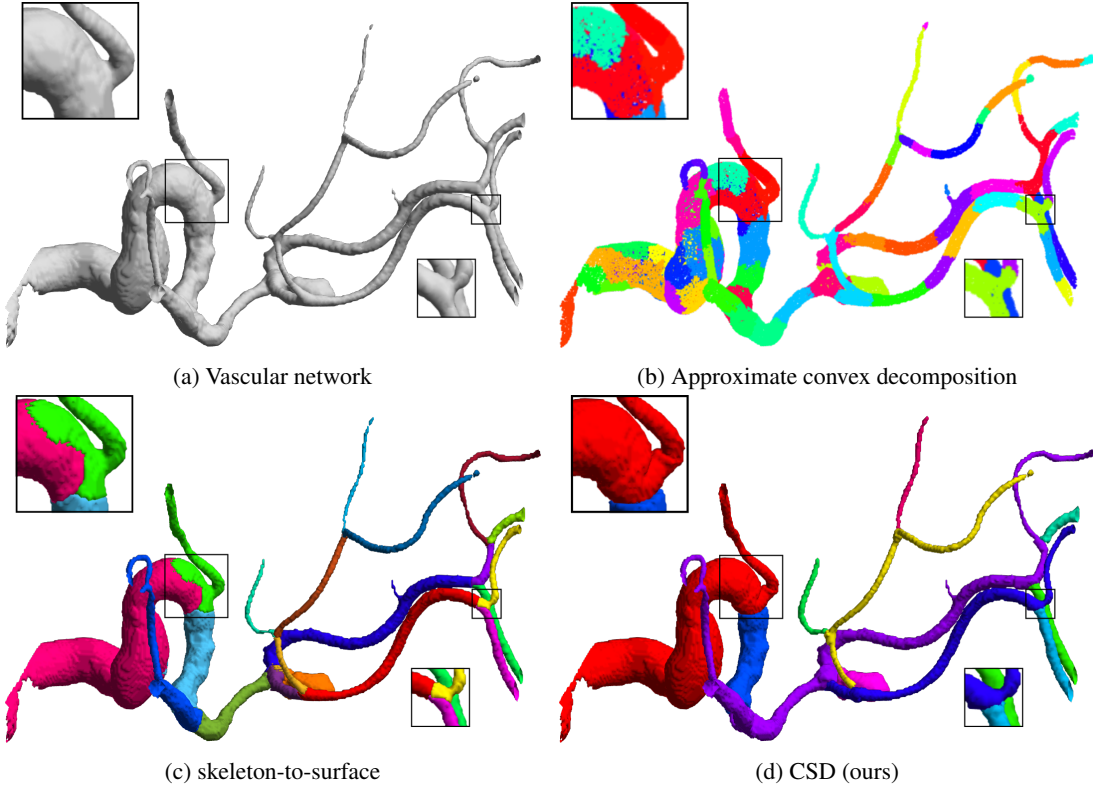


Figure 13: (a) Vascular network as a complex tubular structure with 20 object parts (the skeleton of the vascular network is presented in Fig. 3b). (b) Approximate convex decomposition over-segments the vascular network. (c) Skeleton-to-surface mapping decomposes the object into 20 semantic components, and the boundaries between these components are not accurate. (d) CSD decomposes the object into eight semantic components and reconstructs the object at intersections. Objects inside boxes are magnified. The 3D image of the vascular network is acquired from https://github.com/cbm755/fast_marching_kroon.

8.5. Computation time

The time complexity of the sub-voxel precise skeletonization is $O(n N_\Omega \log N_\Omega)$, where n is the number of skeleton branches, and N_Ω is the number of voxels in a discrete Ω . The $N_\Omega \log N_\Omega$ factor is from the fast marching algorithm [35]. The time complexity to determine a critical point is $O(N_p)$, where N_p is the number of inquiry points that we check for the cross-sectional changes in the corresponding decomposition interval. Defining the critical points is independent of N_Ω . The complexity of the method is measured through the number of basic arithmetic operations performed; other factors that may also influence the execution time, such as the number of memory accesses or memory consumption, have not been considered.

On a $2 \times$ Intel Xeon E5 2 630 CPU 2.4 GHz machine with 512 GB RAM using Python 2.7, the skeletonization of the myelinated axon shown in the first row of Fig. 11 ($N_\Omega = 395\,594$) consumes 117 s and defining its critical points 353 s. Down-sampling the sub-skeletons

with a factor has minimum effect on results but reduces the time for identifying critical points significantly, e.g., down-sampling with a factor 1/5 reduces the time to 75 s. On the same machine, the skeletonization of the synthetic objects shown in Fig. 14 (N_Ω ranges from 10 000 to 20 000) consumes 4–6 s and defining the critical points 8–15 s.

9. Conclusion

In this paper, we propose the application of 3D shape decomposition in image segmentation. We apply the CSD algorithm to rectify under-segmented tubular objects in the foreground segmentation of large image datasets. We drive the decomposition on the skeleton graph of objects to determine their semantic tubular components. For that, we partition the skeleton graph into distinct maximal-length paths over an orientation cost. Each path corresponds to a sub-skeleton, and each sub-skeleton corresponds to a semantic component. To determine the intersection of the semantic

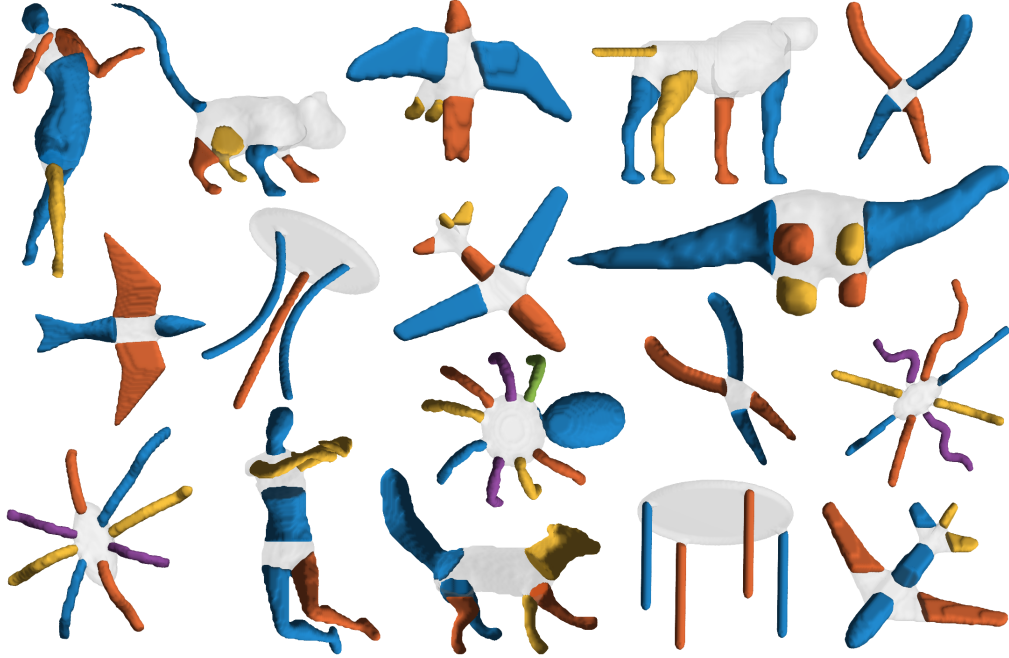


Figure 14: A gallery of CSD decomposition of synthetic objects. Semantic components are given the same color, e.g., the table legs and the wings of birds are one semantic component. The grey-colored partition(s) of the objects shows intersections.

Table 1: The number of object parts, n , semantic components, m , intersections, δ , of objects shown in Fig. 14. The computation time to determine the curve skeleton (Skel time) and critical points (CP time). The order of the objects in the table is based on Fig. 14 from left to right, starting from the top-left object.

Model	n	m	δ	Time (s)	
				Skel time	CP time
Human	6	3	2	4	12
Four limb	5	3	1	4	11
Bird	6	3	1	3	10
Four limb	6	3	1	4	13
Pliers	4	2	1	4	8
Bird	7	2	1	3	10
Table	3	2	1	4	9
Airplane	7	3	2	5	10
Dinosaur	6	3	1	4	10
Spider	9	5	1	6	14
Pliers	4	2	1	4	8
Octopus	8	4	1	6	14
Octopus	9	4	1	6	15
Human	6	3	2	4	12
Four limb	7	3	1	4	11
Table	6	2	1	4	10
Airplane	9	3	2	4	9

components, we propose to sweep the object along sub-skeletons in decomposition intervals and find the critical points. Cutting the object at critical points, we obtain object parts and intersections. We assign the same label to object parts which are along the same sub-skeleton, acquiring a semantic component. We further propose to reconstruct the semantic components at intersections using generalized cylinders. We demonstrate the application of CSD for the segmentation of large 3D-EM datasets of myelinated axons, the decomposition of vascular networks, as well as synthetic objects. Comparing CSD to other state-of-the-art decomposition techniques in these applications shows that CSD outperforms these techniques.

Acknowledgements

This work was supported by the Academy of Finland (grant 316258 to J.T. and grant 323385 to A.S.). The authors acknowledge CSC-IT Center for Science, Finland, and Bioinformatics Center, University of Eastern Finland, Finland, for computational resources.

Competing interests

The authors declare that they have no conflict of interest.

Availability of data and material

The source code of the CSD algorithm will be available at https://github.com/aAbdz/cylindrical_shape_decomposition.

References

- [1] O. V. Kaick, N. Fish, Y. Kleiman, S. Asafi, D. Cohen-OR, Shape Segmentation by Approximate Convexity Analysis, *ACM Transactions on Graphics* 34 (1) (2015) 1–11. [doi:10.1145/2611811](https://doi.org/10.1145/2611811).
- [2] Y. Zhou, K. Yin, H. Huang, H. Zhang, M. Gong, D. Cohen-Or, Generalized cylinder decomposition, *ACM Transactions on Graphics* 34 (6) (2015) 1–14. [doi:10.1145/2816795.2818074](https://doi.org/10.1145/2816795.2818074).
- [3] O. K. C. Au, C. L. Tai, H. K. Chu, D. Cohen-Or, T. Y. Lee, Skeleton extraction by mesh contraction, *SIGGRAPH'08: International Conference on Computer Graphics and Interactive Techniques, ACM SIGGRAPH 2008 Papers* 2008.
- [4] S. Beretti, A. Del Bimbo, P. Pala, *3D Mesh decomposition using Reeb graphs*, *Image and Vision Computing* 27 (10) (2009) 1540–1554. [doi:10.1016/j.imavis.2009.02.004](https://doi.org/10.1016/j.imavis.2009.02.004).
URL <http://dx.doi.org/10.1016/j.imavis.2009.02.004>
- [5] E. Zuckerman, A. Tal, S. Shlafman, Polyhedral surface decomposition with applications, *Computers and Graphics (Pergamon)* 26 (5) (2002) 733–743. [doi:10.1016/S0097-8493\(02\)00128-0](https://doi.org/10.1016/S0097-8493(02)00128-0).
- [6] K. Siddiqi, J. Zhang, D. Macrini, A. Shokoufandeh, S. Bouix, S. Dickinson, Retrieving articulated 3-D models using medial surfaces, *Machine Vision and Applications* 19 (4) (2008) 261–275. [doi:10.1007/s00138-007-0097-8](https://doi.org/10.1007/s00138-007-0097-8).
- [7] M. Goyal, S. Murugappan, C. Piya, W. Benjamin, Y. Fang, M. Liu, K. Ramani, *Towards locally and globally shape-aware reverse 3D modeling*, *CAD Computer Aided Design* 44 (6) (2012) 537–553. [doi:10.1016/j.cad.2011.12.004](https://doi.org/10.1016/j.cad.2011.12.004).
URL <http://dx.doi.org/10.1016/j.cad.2011.12.004>
- [8] M. Averkiou, V. G. Kim, Y. Zheng, N. J. Mitra, ShapeSynth: Parameterizing model collections for coupled shape exploration and synthesis, *Computer Graphics Forum* 33 (2) (2014) 125–134. [doi:10.1111/cgf.12310](https://doi.org/10.1111/cgf.12310).
- [9] T. Funkhouser, M. Kazhdan, P. Shilane, P. Min, W. Kiefer, A. Tal, S. Rusinkiewicz, D. Dobkin, Modeling by example, *ACM SIGGRAPH 2004 Papers, SIGGRAPH 2004* (2004) 652–663. [doi:10.1145/1186562.1015775](https://doi.org/10.1145/1186562.1015775).
- [10] G. D. Rubin, J. Leipsic, U. Joseph Schoepf, D. Fleischmann, S. Napel, CT angiography after 20 years: A transformation in cardiovascular disease characterization continues to advance, *Radiology* 271 (3) (2014) 633–652. [doi:10.1148/radiol.14132232](https://doi.org/10.1148/radiol.14132232).
- [11] M. Berning, K. M. Boergens, M. Helmstaedter, SegEM: Efficient Image Analysis for High-Resolution Connectomics, *Neuron* 87 (6) (2015) 1193–1206. [doi:10.1016/j.neuron.2015.09.003](https://doi.org/10.1016/j.neuron.2015.09.003).
- [12] Z. Zheng, J. S. Lauritzen, E. Perlman, C. G. Robinson, M. Nichols, D. Milkie, O. Torrens, J. Price, C. B. Fisher, N. Sharifi, S. A. Calle-Schuler, L. Kmecova, I. J. Ali, B. Karsh, E. T. Trautman, J. A. Bogovic, P. Hanslovsky, G. S. Jefferis, M. Kazhdan, K. Khairy, S. Saalfeld, R. D. Fetter, D. D. Bock, *A Complete Electron Microscopy Volume of the Brain of Adult Drosophila melanogaster*, *Cell* 174 (3) (2018) 730–743. [doi:10.1016/j.cell.2018.06.019](https://doi.org/10.1016/j.cell.2018.06.019).
URL <https://doi.org/10.1016/j.cell.2018.06.019>
- [13] A. Lucchi, K. Smith, R. Achanta, G. Knott, P. Fua, Supervoxel-based segmentation of mitochondria in em image stacks with learned shape features, *IEEE Transactions on Medical Imaging* 31 (2) (2012) 474–486. [doi:10.1109/TMI.2011.2171705](https://doi.org/10.1109/TMI.2011.2171705).
- [14] J. Nunez-Iglesias, R. Kennedy, S. M. Plaza, A. Chakraborty, W. T. Katz, Graph-based Active Learning of Agglomeration (GALA): A python library to segment 2D and 3D neuroimages, *Frontiers in Neuroinformatics* 8 (APR) (2014) 1–6. [doi:10.3389/fninf.2014.00034](https://doi.org/10.3389/fninf.2014.00034).
- [15] J. Funke, F. Tschopp, W. Grisaitis, A. Sheridan, C. Singh, S. Saalfeld, S. C. Turaga, Large Scale Image Segmentation with Structured Loss Based Deep Learning for Connectome Reconstruction, *IEEE Transactions on Pattern Analysis and Machine Intelligence* 41 (7) (2019) 1669–1680. [doi:10.1109/TPAMI.2018.2835450](https://doi.org/10.1109/TPAMI.2018.2835450).
- [16] S. Moccia, E. De Momi, S. El Hadji, L. S. Mattos, *Blood vessel segmentation algorithms: Review of methods, datasets and evaluation metrics*, *Computer Methods and Programs in Biomedicine* 158 (2018) 71–91. [doi:10.1016/j.cmpb.2018.02.001](https://doi.org/10.1016/j.cmpb.2018.02.001).
URL <https://doi.org/10.1016/j.cmpb.2018.02.001>
- [17] A. Abdollahzadeh, I. Belevich, E. Jokitalo, J. Tohka, A. Sierra, Automated 3D Axonal Morphometry of White Matter, *Scientific Reports* 9 (1) (2019) 6084. [doi:10.1038/s41598-019-42648-2](https://doi.org/10.1038/s41598-019-42648-2).
- [18] A. F. Frangi, W. J. Niessen, K. L. Vincken, M. A. Viergever, *Multiscale vessel enhancement filtering*, in: W. Wells, A. Colchester, S. Delp (Eds.), *Medical Image Computing and Computer-Assisted Intervention - MICCAI98*. MICCAI 1998. Lecture Notes in Computer Science, Springer, Berlin, Heidelberg, 1998, pp. 130–137. [doi:10.1007/BFb0056195](https://doi.org/10.1007/BFb0056195).
URL <http://link.springer.com/10.1007/BFb0056195>
- [19] M. W. K. Law, A. C. S. Chung, Three Dimensional Curvilinear Structure Detection Using Optimally Oriented Flux, in: *Computer Vision - ECCV 2008*, Springer Berlin Heidelberg, Berlin, Heidelberg, 2008, pp. 368–382. [doi:10.1007/978-3-540-88693-8__27](https://doi.org/10.1007/978-3-540-88693-8__27).
- [20] E. Franken, R. Duits, Crossing-preserving coherence-enhancing diffusion on invertible orientation scores, *International Journal of Computer Vision* 85 (3) (2009) 253–278. [doi:10.1007/s11263-009-0213-5](https://doi.org/10.1007/s11263-009-0213-5).
- [21] J. Hamink, R. Duits, E. Bekkers, Crossing-preserving multiscale vesselness, *Medical image computing and computer-assisted intervention : MICCAI ... International Conference on Medical Image Computing and Computer-Assisted Intervention* 17 (2014) 603–610. [doi:10.1007/978-3-319-10470-6__35](https://doi.org/10.1007/978-3-319-10470-6__35).
- [22] P. Liskowski, K. Krawiec, Segmenting Retinal Blood Vessels with Deep Neural Networks, *IEEE Transactions on Medical Imaging* 35 (11) (2016) 2369–2380. [doi:10.1109/TMI.2016.2546227](https://doi.org/10.1109/TMI.2016.2546227).
- [23] D. Reniers, J. J. van Wijk, A. Telea, Computing Multiscale Curve and Surface Skeletons of Genus 0 Shapes Using a Global Importance Measure, *IEEE Transactions on Visualization and Computer Graphics* 14 (2) (2008) 355–368. [doi:10.1109/TVCG.2008.23](https://doi.org/10.1109/TVCG.2008.23).
- [24] P. D. Simari, K. Singh, Extraction and Remeshing of Ellipsoidal Representations from Mesh Data, in: *Proceedings of Graphics Interface 2005*, Canadian Human-Computer Communications

- Society, Victoria, British Columbia, 2005, p. 161168.
- [25] R. RAAB, C. GOTSMAN, A. SHEFFER, Virtual Woodwork: Making Toys From Geometric Models, International Journal of Shape Modeling 10 (01) (2004) 1–29. [doi:10.1142/s0218654304000584](https://doi.org/10.1142/s0218654304000584).
- [26] M. Mortal, G. Patanè, M. Spagnuolo, B. Falcidieno, J. Rossignac, Plumber: A method for a multi-scale decomposition of 3D shapes into tubular primitives and bodies, in: ACM Symposium on Solid Modeling and Applications, SM, 2004, pp. 339–344. [doi:10.2312/sm.20041412](https://doi.org/10.2312/sm.20041412).
- [27] S. Asafi, A. Goren, D. Cohen-Or, Weak convex decomposition by lines-of-sight, Eurographics Symposium on Geometry Processing 32 (5) (2013) 23–31. [doi:10.1111/cgf.12169](https://doi.org/10.1111/cgf.12169).
- [28] X. Li, T. W. Toon, Z. Huang, Decomposing polygon meshes for interactive applications, in: Proceedings of the 2001 symposium on Interactive 3D graphics - SI3D '01, ACM Press, New York, New York, USA, 2001, pp. 35–42. [doi:10.1145/364338.364343](https://doi.org/10.1145/364338.364343).
- [29] I. Biederman, Recognition-by-Components: A Theory of Human Image Understanding An Analogy Between Speech and Object Perception, Psychological Review M (2) (1971) 115–147.
- [30] P. D. Grünwald, The Minimum Description Length Principle (Adaptive Computation and Machine Learning), The MIT Press, 2007.
- [31] N. D. Cornea, D. Silver, P. Min, Curve-skeleton properties, applications, and algorithms, IEEE Transactions on Visualization and Computer Graphics 13 (3) (2007) 530–548. [doi:10.1109/TVCG.2007.1002](https://doi.org/10.1109/TVCG.2007.1002).
- [32] A. Lieutier, Any open bounded subset of R^n has the same homotopy type as its medial axis, CAD Computer Aided Design 36 (11) (2004) 1029–1046. [doi:10.1145/781606.781620](https://doi.org/10.1145/781606.781620).
- [33] M. Sabry Hassouna, A. A. Farag, Robust centerline extraction framework using level sets, Proceedings - 2005 IEEE Computer Society Conference on Computer Vision and Pattern Recognition, CVPR 2005 I (2005) 458–467. [doi:10.1109/CVPR.2005.306](https://doi.org/10.1109/CVPR.2005.306).
- [34] R. Van Uitert, I. Bitter, Subvoxel precise skeletons of volumetric data based on fast marching methods, Medical physics 34 (2) (2007) 627–638. [doi:10.1118/1.2409238](https://doi.org/10.1118/1.2409238).
- [35] J. A. Sethian, A fast marching level set method for monotonically advancing fronts., Proceedings of the National Academy of Sciences 93 (4) (1996) 1591–1595. [doi:10.1073/pnas.93.4.1591](https://doi.org/10.1073/pnas.93.4.1591).
URL <http://www.pnas.org/cgi/doi/10.1073/pnas.93.4.1591>
- [36] F. Chazal, A. Lieutier, J. Rossignac, Projection-homeomorphic surfaces, ACM Symposium on Solid Modeling and Applications, SM (2005) 9–14 [doi:10.1145/1060244.1060247](https://doi.org/10.1145/1060244.1060247).
- [37] U. Shani, D. H. Ballard, Splines as embeddings for generalized cylinders, Computer Vision, Graphics, and Image Processing 27 (2) (1984) 129–156. [doi:https://doi.org/10.1016/S0734-189X\(84\)80039-0](https://doi.org/10.1016/S0734-189X(84)80039-0).
- [38] D. H. Ballard, C. M. Brown, Computer Vision, 1st Edition, Prentice Hall Professional Technical Reference, 1982.
- [39] A. Abdollahzadeh, I. Belevich, E. Jokitalo, A. Sierra, J. Tohka, DeepACSON: Automated Segmentation of White Matter in 3D Electron Microscopy, bioRxiv [doi:https://doi.org/10.1101/828541](https://doi.org/10.1101/828541).